

Retraction

Retracted: Research on Mapping Error Control of Underground Space Mobile LiDAR Constrained by Cooperative Targets

Journal of Sensors

Received 23 January 2024; Accepted 23 January 2024; Published 24 January 2024

Copyright © 2024 Journal of Sensors. This is an open access article distributed under the Creative Commons Attribution License, which permits unrestricted use, distribution, and reproduction in any medium, provided the original work is properly cited.

This article has been retracted by Hindawi following an investigation undertaken by the publisher [1]. This investigation has uncovered evidence of one or more of the following indicators of systematic manipulation of the publication process:

- (1) Discrepancies in scope
- (2) Discrepancies in the description of the research reported
- (3) Discrepancies between the availability of data and the research described
- (4) Inappropriate citations
- (5) Incoherent, meaningless and/or irrelevant content included in the article
- (6) Manipulated or compromised peer review

The presence of these indicators undermines our confidence in the integrity of the article's content and we cannot, therefore, vouch for its reliability. Please note that this notice is intended solely to alert readers that the content of this article is unreliable. We have not investigated whether authors were aware of or involved in the systematic manipulation of the publication process.

Wiley and Hindawi regrets that the usual quality checks did not identify these issues before publication and have since put additional measures in place to safeguard research integrity.

We wish to credit our own Research Integrity and Research Publishing teams and anonymous and named external researchers and research integrity experts for contributing to this investigation.

The corresponding author, as the representative of all authors, has been given the opportunity to register their agreement or disagreement to this retraction. We have kept a record of any response received.

References

- [1] H. Liu, Y. Li, B. Wang, and Z. Guo, "Research on Mapping Error Control of Underground Space Mobile LiDAR Constrained by Cooperative Targets," *Journal of Sensors*, vol. 2022, Article ID 8690532, 12 pages, 2022.

Research Article

Research on Mapping Error Control of Underground Space Mobile LiDAR Constrained by Cooperative Targets

Huiyun Liu ¹, Yongqiang Li ¹, Baoshan Wang ¹ and Zengzhang Guo ²

¹Henan Polytechnic University, School of Surveying and Land Information Engineering, Jiaozuo, 454003 Henan Province, China

²Henan College of Surveying and Mapping, Zhengzhou, 454500 Henan Province, China

Correspondence should be addressed to Huiyun Liu; liuhuiyun@hpu.edu.cn

Received 26 July 2022; Accepted 16 September 2022; Published 10 October 2022

Academic Editor: Yuan Li

Copyright © 2022 Huiyun Liu et al. This is an open access article distributed under the Creative Commons Attribution License, which permits unrestricted use, distribution, and reproduction in any medium, provided the original work is properly cited.

In the underground environment, it is difficult to obtain spatial three-dimensional data because of occlusion and its complexity. Mobile light detection and ranging (LiDAR) measurement technology has the ability to obtain three-dimensional spatial information quickly and accurately, but in the underground environment, because of the lack of global navigation satellite system (GNSS) signal in the integrated navigation system, the measurement accuracy decreases with the increase of time. In this paper, an extended Kalman filter-based loose mode is constructed using the real coordinates of the center of gravity of the target and the measurement information of the laser foothold. It provides an additional space-time reference for the integrated navigation system of the mobile LiDAR system and restricts the errors. The simulation results show that the proposed method can effectively improve the measurement accuracy of mobile LiDAR system and enhance the 3D spatial perception ability of underground space.

1. Introduction

Traditional underground space measurement mainly adopts engineering measurement methods such as total station, measuring robot, artificial static and discrete observation [1–3], and cloud point/image [4–6]. Among them, total station, measuring robot has high accuracy and good reliability, which can reach the millimeter level. The accuracy of photogrammetry can reach decimeter level. However, when traditional measurement methods obtain data, they face many problems such as low efficiency, poor safety of surveyors, and high cost of manpower and material resources, the accuracy of information acquisition is not high, and the details are incomplete [3]. The acquisition method of underground space information is inconsistent with the current demand for reliable, accurate, and fast acquisition of three-dimensional underground space information. Mobile light detection and ranging (LiDAR) technology has the advantages of fast data acquisition speed and high precision and has been widely used in 3D spatial information acquisition. Mobile LiDAR technology adopts the active measurement

method, which does not depend on illumination and can efficiently obtain 3D data of underground space. However, the mobile LiDAR system relies on the accurate pose information of position and orientation system (POS). When outdoor global navigation satellite system (GNSS) signals are good, POS system can provide centimeter-level positioning accuracy [7]. In the underground space, the GNSS signals are weak or blocked, resulting in mobile LiDAR measurement data quality over time cannot meet the measurement accuracy requirements [8–10].

Although mobile LiDAR technology has been applied in underground spatial information measurement, there are still challenges for large-scale 3D data acquisition in long tunnels and indoor spaces without GNSS signals due to the lack of significant features or complex environments. The current research on the rapid acquisition and mapping of underground space information can be divided into four categories: mobile measurement system for measuring and its improvement [11–21], laser based on simultaneous localization and mapping (SLAM) algorithm [22–25], monocular/binocular vision sensor [26], and RGBD (Red, Green, Blue,

Depth map) vision sensor mobile robot system [27–30] and its corresponding unmanned aerial vehicle (UAV) [31–35] platform.

The improved underground space information acquisition equipment based on the traditional mobile measurement system has the advantages of high relative accuracy, no need to form a closed-loop condition, and small error accumulation of long-time data acquisition. However, it also has the disadvantages of low automation, no real-time processing, and extra work. The acquisition of spatial data in underground and indoor areas without GNSS signal based on SLAM system has the advantages of high automation, good real-time data, and fast acquisition speed. However, this method also has the disadvantages of large relative errors of data and large accumulation of long-time acquisition errors, especially in special environments with no closed loop for a long time, insignificant features, or dynamic changes in space.

In GNSS-denied environment, the traditional vehicle robots used for underground space positioning have high precision, but it is difficult to achieve high dynamic continuous positioning [36]. Although the radio frequency identification (RFID) [37], ZigBee technology [38], infrared technology [39], Bluetooth [40], Ultra Wideband Technology (UWB) [41], Wi-Fi, and other wireless positioning method developed in recent years can solve the problem of dynamic positioning, it has low precision, small coverage, and high cost. Another underground space positioning method, pseudostar positioning can achieve centimeter-level accuracy when the signal is good, but the signal is easily interfered, and it is not suitable for positioning in long linear space such as subway tunnel [42].

In this paper, the authors analyzed the measurement error characteristics of the mobile LiDAR and then constructed the GNSS/IMU (inertial measurement unit)/target observation based on the current research. The cooperative targets are arranged to restrain the error drift of the mobile measurement system. The simulation experiment is analyzed and verified, and the appropriate target spacing is given for reference.

2. Theory of Method

Kalman filter (KF) is an optimal estimation algorithm based on hidden Markov model, which is simple and easy, and has been widely used in navigation, control, and data fusion. The recursive method is adopted to update the state estimate through the weighted average of the observation data and the prior values, without storing the measured values during the whole observation process. Therefore, KF is suitable for dynamic modeling. In the discrete Kalman filter, its state equation and measurement equation are shown in

$$\begin{cases} X_k = \Phi_{k/k-1} X_{k-1} + \Gamma_{k/k-1} W_{k-1}, \\ Z_k = H_k X_k + V_k, \end{cases} \quad (1)$$

where X_k is the state vector, the dimension is $n \times 1$; Z_k is the measurement vector, the dimension is $m \times 1$; $\Phi_{k/k-1}$,

$\Gamma_{k/k-1}$, and H_k are, respectively, the state transition matrix ($n \times n$), system noise allocation matrix ($n \times l$), and measurement matrix ($m \times n$) at the corresponding moment; W_{k-1} and V_k are, respectively, the system noise vector ($l \times 1$) and the measurement noise vector ($m \times 1$); they are Gaussian white noises which are not correlated with each other, satisfying the expected normal distribution of zero.

In the mobile LiDAR system, the accuracy of the point cloud is mainly determined by the spatiotemporal reference provided by POS. To solve the problem of accurate acquisition of point cloud data in the environment of poor GNSS signal or missing, three-dimensional cooperative target is used to provide the spatiotemporal reference for the trajectory, and the extended Kalman filter (EKF) algorithm is used for data fusion to improve the trajectory calculation accuracy and reduce the error drift. However, for the navigation system composed of GNSS, IMU, and target, the state vector transfer and the conversion between observation quantity and state quantity are strongly nonlinear. The Kalman filter algorithm is only applicable to the linear data and cannot be directly used to process the nonlinear data.

For the extended Kalman filter in nonlinear space, the premise is to assume a model for the discrete state space and replace the system state matrix and observation matrix of the standard model with a nonlinear function.

$$\begin{cases} X_k = f(X_{k-1}) + \Gamma_{k-1} W_{k-1}, \\ Z_k = h(X_k) + V_k, \end{cases} \quad (2)$$

where W_{k-1} and V_k are system noise and observation noise; they both obey Gaussian white noise with a mean value of zero. $\Gamma_{k/k-1}$ system noise allocation matrix ($n \times l$). $f(X_k)$ and $h(X_k)$ are m - and n -dimensional nonlinear vector functions, respectively.

The system transfer functions $f(x)$ and $h(x)$ in the system state equation are expanded by first-order Taylor series, respectively, and the first-order terms are reserved for approximation. A new linear system and an indirect filtering system are formed by state deviation and measurement deviation, and then, the best state is estimated by Kalman filter. The filtering model is as follows:

$$\begin{cases} \Delta X_k^- = \Phi_{k/k-1} \Delta X_{k-1}^+, \\ P_k^- = \Phi_{k/k-1} P_{k-1}^+ \Phi_{k/k-1}^T + \Gamma_{k/k-1} Q_{k-1} \Gamma_{k/k-1}^T, \\ K_k = P_k^- H_k^T (H_k P_k^- H_k^T + R_k)^{-1}, \\ \Delta X_k^+ = \Delta X_k^- + K_k (Z_k - H_k \Delta X_k^-), \\ P_k^+ = (I - K_k H_k) P_k^-, \end{cases} \quad (3)$$

where ΔX_k^- is the difference of the state vector estimated value from ΔX_{k-1}^+ to ΔX_k^- ; $\Phi_{k/k-1}$ is the Jacobian matrix corresponding to the nonlinear vector equation $f(x)$. P_k^- is the covariance matrix from P_{k-1}^+ to P_k^- ; K_k is the Kalman filter gain matrix; H_k is the Jacobian matrix corresponding to the nonlinear vector equation $h(x)$. ΔX_k^+ is the state estimation value difference updated from ΔX_k^- to ΔX_k^+ ; P_k^+ is the

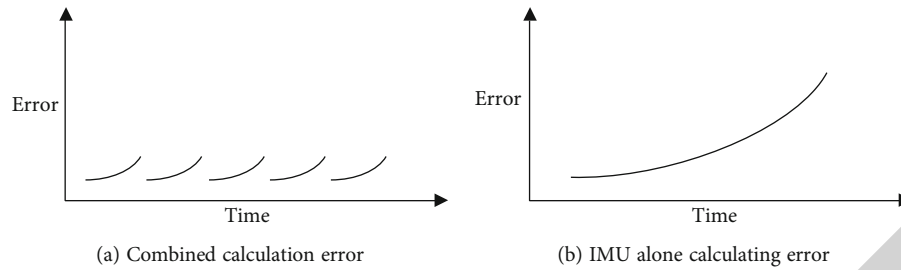


FIGURE 1: POS integrated navigation solution error characteristics.

error covariance matrix from P_k^- to P_k^+ update. Q_{k-1} and R_k are the system noise covariance matrix and the observation noise covariance matrix at the corresponding filter moment, respectively.

According to the optimal estimation of state deviation and initial state value at time K , the optimal state estimation value at time K can be calculated as

$$X_k = \Delta X_k + X_k^-, \quad (4)$$

or

$$X_k = \Delta X_k + f(X_{k-1}^0). \quad (5)$$

3. Error Analysis of Mobile LiDAR for Underground Space

The mobile LiDAR system is a measurement system integrated with multiple sensors such as GNSS, IMU, and laser scanners. When the mobile LiDAR system is used to obtain scene information such as underground space and indoors, there are measurement errors due to many factors. The error sources are mainly divided into laser measurement error, spatiotemporal synchronization error, target system error, and integrated navigation error. Laser scanner has relatively high measurement accuracy, and the measurement error is generally within 2 cm, within the limited measurement distance such as indoor and underground space, which has limited impact on the overall measurement. Laser scanners can be corrected by laser ranging so that their errors become random noise of a smaller magnitude [42]. The spatiotemporal synchronization error includes the spatial synchronization error caused by the eccentricity and the installation angle error of the multisensor integration and the time synchronization error corresponding to the time reference of each sensor. In many literatures and researches, the error of spatial synchronization is treated as a kind of systematic error [43] and calibrated through self-calibration [44–48] or control point-based calibration methods [49–52]. Spatial synchronization can obtain the precise geometric transformation relationship among the sensors through the calibration method, which can reduce or even eliminate the error. The time synchronization error is caused by the performance difference and sampling frequency difference of various sensors, which can be effectively contained by the precise time synchronization and frequency difference. The

spatiotemporal synchronization error can generally be controlled within 1-2 cm, which has a limited influence on the overall measurement. The positioning and orientation system (POS) error is the most difficult one to deal with, which is closely related to the environment, like denied the GNSS signals [42]. Cooperative target error is an extra error introduced in underground and indoor spaces to restrict spatial positioning and provide spatial reference. This error does not include a system error, and its error is considered as an accidental error. Moreover, the target data has high accuracy and the navigation system related data has low accuracy; the final result can meet the accuracy requirements of the underground navigation system by introducing target data into the navigation system to control the overall navigation error. The cooperative target adopts sensitive materials with good reflectivity to laser pulses and selects easy-to-recognize graphics, which is conducive to automatically identify the center position of the target from the laser point cloud. A large number of studies have been carried out in this area, among which the robust target center positioning algorithm based on M estimation [13] can achieve the target center positioning of 1-2 mm. In addition, the absolute position of the target is accurately measured by the precision total station, and the error is generally less than 2 cm, so it can be seen that the cooperative target error has limited influence on the overall measurement. In the mobile LiDAR system, in the loosely coupled mode of GNSS/IMU integrated navigation system, smoothing the POS trajectory can achieve relatively accurate spatial positioning and attitude determination, and the error presents a certain periodicity (Figure 1(a)), but the overall error is relatively small, generally within 1-5 cm. However, in the underground and indoor blind environment, GNSS signals are missing, and the pose of the mobile LiDAR system is independently provided by IMU, which will rapidly bring very serious accumulated errors with the increase of time (Figure 1(b)). It can be seen that in the underground blind environment, the effective containment and correction of IMU estimation errors have become the primary task to solve the underground space positioning.

4. Trajectory Correction Model of Mobile LiDAR with Cooperative Target Constraints

In the underground space without GNSS signals, the mobile LiDAR system has no significant difference in point cloud acquisition error and spatiotemporal synchronization error

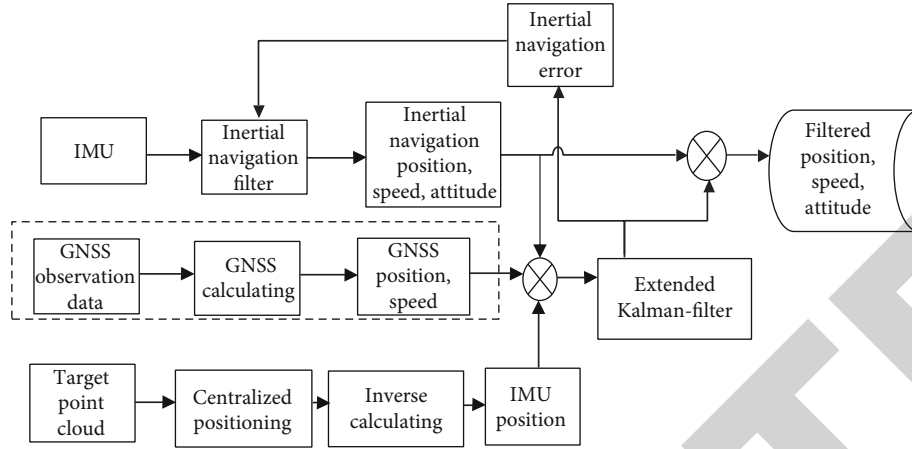


FIGURE 2: POS location loose coupling model with graphic target constraints.

with the outdoor GNSS signal in good condition. However, in the integrated navigation error, because there is no GNSS, it only relies on IMU for trajectory estimation, and the error cannot be effectively controlled and increases sharply. When the mobile LiDAR system obtains underground space information, it usually adopts a method similar to the ground environment, which requires the participation of GNSS. However, after entering the blind environment, GNSS signal disappears. When the data is solved, GNSS will no longer participate in the relevant calculations due to the absence of reliable GNSS signal. This study is based on the extended Kalman filter algorithm using the loose coupling mode and derives the trajectory error solution model based on the graphical target constraint (Figure 2).

4.1. IMU Trajectory State Model. Among the measurement errors of gyroscope and accelerometer in the IMU, the installation errors and the scale factor errors can be measured and compensated. Considering the simplicity of the system, only the random errors that cannot be compensated are described.

Differential equation of attitude error:

$$\dot{\phi} = \phi \times \omega_{in}^n + \delta\omega_{in}^n - \delta\omega_{ib}^b, \quad (6)$$

where ϕ is the attitude error function. $\delta\omega_{in}^n$ is the error between the calculated navigation coordinate system of the strapdown inertial navigation and the actual navigation coordinate system, and $\delta\omega_{ib}^b$ is the error generated by the gyroscope measurement.

In the navigation coordinate system, the differential equation of velocity error is

$$\delta\dot{v}^n = f_{sf}^n \times \phi + v^n \times (2\delta\omega_{ie}^n + \delta\omega_{en}^n) - (\omega_{ie}^n + \omega_{en}^n) \times \delta v^n + \delta f_{sf}^b + \delta g^n, \quad (7)$$

where δf_{sf}^b is the error generated by the acceleration measurement difference, $\delta\omega_{ie}^n$ is the calculation error of the earth rotation speed, $\delta\omega_{en}^n$ is the calculation error of the navigation system rotation relative to the earth-fixed coordinate system,

and δg^n is the gravity model error. The above error calculation formulas are as follows:

$$\begin{aligned} \delta f_{sf}^b &= \tilde{f}_{sf}^b - f_{sf}^b, \\ \delta\omega_{ie}^n &= \tilde{\omega}_{ie}^n - \omega_{ie}^n, \\ \delta\omega_{en}^n &= \tilde{\omega}_{en}^n - \omega_{en}^n, \\ \delta g &= \tilde{g}^n - g^n. \end{aligned} \quad (8)$$

The position error differential equation has different forms in different directions, which are

$$\begin{cases} \delta\dot{L} = \frac{1}{R_M + h} \delta v_n - \frac{v_N}{(R_M + h)^2} \delta h, \\ \delta\dot{\lambda} = \frac{\sec L}{R_N + h} \delta v_E + \frac{v_E \sec L \tan L}{R_N + h} \delta L - \frac{v_E \sec L}{(R_N + h)^2} \delta h, \\ \delta\dot{h} = \delta v_H, \end{cases} \quad (9)$$

where L and λ are longitude and latitude and v_N , v_E , and v_H , respectively, are the projections of velocity in the three directions of the local coordinate system. The IMU sensor error model in this paper includes gyroscope drift error and accelerometer error, and its error differential equation is

$$\begin{cases} \dot{\varepsilon}_b = 0, \\ \dot{\varepsilon}_r = -\frac{1}{T} \varepsilon_r + \omega_r, \\ \dot{\Delta} = -\frac{1}{T} \Delta + \omega_a, \end{cases} \quad (10)$$

where ε_b is the random drift of the gyroscope, ε_r is the first-order Markov process of the gyroscope error, T is the correlation time, and Δ is the accelerometer measurement error.

According to the IMU attitude error equation (Equation (6)), velocity error equation (Equation (7)), position error equation (Equation (9)), and IMU sensor error (Equation

(10)), the motion state equation of Kalman filter is constructed. In the equation of state, attitude error, velocity error, position error, and IMU sensor error, a total of 18-dimensional parameters are the components of the state parameters, as shown in

$$X = [\varphi \quad v \quad p \quad \varepsilon_b \quad \varepsilon_r \quad \Delta_g]^T, \quad (11)$$

$$\begin{cases} \varphi = [\varphi_E \quad \varphi_N \quad \varphi_H], \\ v = [v_E \quad v_N \quad v_H], \\ p = [p_E \quad p_N \quad p_H], \\ \varepsilon_b = [\varepsilon_x \quad \varepsilon_y \quad \varepsilon_z], \\ \varepsilon_r = [\varepsilon_x \quad \varepsilon_y \quad \varepsilon_z], \\ \Delta_g = [\Delta_x \quad \Delta_y \quad \Delta_z]. \end{cases} \quad (12)$$

The general expression of IMU motion state equation is

$$\dot{X} = F(t)X(t) + G(t)W(t). \quad (13)$$

In the expression, $F(t)$ is the state transition matrix corresponding to the state equation, for any moment t ,

$$F = \begin{bmatrix} F_N & F_s \\ 0 & F_M \end{bmatrix}, \quad (14)$$

where F_N is the system dynamic matrix with 9 parameters of attitude, speed, and position. F_s is a matrix of 9×9 , and its form in the strapdown inertial navigation system is

$$F_s = \begin{bmatrix} C_b^t & C_b^t & 0_{3 \times 3} \\ & C_b^t & \\ 0_{6 \times 6} & 0_{3 \times 3} \end{bmatrix}_{9 \times 9}, \quad (15)$$

where C_b^t is the attitude transformation matrix between the local geographic coordinate system and the platform coordinate system. F_s is a matrix of 9×9 , and its form in the strapdown inertial navigation system is

$$F_s = \begin{bmatrix} C_b^t & C_b^t & 0_{3 \times 3} \\ & C_b^t & \\ 0_{6 \times 6} & 0_{3 \times 3} \end{bmatrix}_{9 \times 9}, \quad (16)$$

where F_M is the state transition parameter of the inertial navigation model, and its specific form is a diagonal matrix

$$F_M = \text{diag} \left[0_{1 \times 3} \quad -\frac{1}{T_{gx}} \quad -\frac{1}{T_{gy}} \quad -\frac{1}{T_{gz}} \quad -\frac{1}{T_{ax}} \quad -\frac{1}{T_{ay}} \quad -\frac{1}{T_{az}} \right], \quad (17)$$

where T_{gx}, T_{gy}, T_{gz} is the time of the gyroscope in the x, y, z direction and T_{ax}, T_{ay}, T_{az} is the time of the acceleration in the x, y, z direction.

$G(t)$ is the control vector function of system noise in the state matrix, and at any time t is

$$G = \begin{bmatrix} C_b^t & 0_{3 \times 3} & 0_{3 \times 3} \\ 0_{3 \times 3} & 0_{3 \times 3} & 0_{3 \times 3} \\ 0_{3 \times 3} & I_{3 \times 3} & 0_{3 \times 3} \\ 0_{3 \times 3} & 0_{3 \times 3} & I_{3 \times 3} \end{bmatrix}_{18 \times 9}. \quad (18)$$

$W(t)$ is the noise matrix

$$W = [\omega_{gx} \quad \omega_{gy} \quad \omega_{gz} \quad \omega_{bx} \quad \omega_{by} \quad \omega_{bz} \quad \omega_{ax} \quad \omega_{ay} \quad \omega_{az}]^T, \quad (19)$$

where $\omega_{gx}, \omega_{gy}, \omega_{gz}, \omega_{bx}, \omega_{by}, \omega_{bz}, \omega_{ax}, \omega_{ay}, \omega_{az}$ is the white noise of the gyroscope, sensor platform, and accelerometer in the x, y, z direction.

4.2. Mobile LiDAR Trajectory Observation Model. GNSS and IMU form an integrated navigation system. In the indirect Kalman filter mode, the IMU track estimation results are taken as the initial observation, and GNSS observation results are taken as the information to calculate the track estimation errors, and then, the navigation results are obtained. GNSS observations and IMU measurements are carried out independently of each other, and there is no correlation. Meanwhile, due to the limitation of physical conditions, the antenna center of GNSS receiver does not coincide with the coordinate center of IMU, so it is necessary to calculate the result of GNSS difference decomposition into the IMU coordinate system, to participate in the combined solution of GNSS/IMU/target. The target center coordinates are obtained in other ways and correspond to the UTC time of POS trajectory, but there is still a difference between the target center point cloud and the coordinate system of POS measurement center. Therefore, it needs to be calculated inversely according to the LiDAR positioning equation to obtain the corresponding IMU position at the moment, which participate in the GNSS/IMU/target combination calculation.

4.2.1. GNSS Observation. The position results of GNSS differential observations are normalized to the IMU coordinate system through an arm effect, as shown in Figure 3.

The reduced equation is

$$\delta l = r_{\text{GNSS}}^e - R_{\text{IMU}}^e, \quad (20)$$

where δl is the arm length vector from IMU to GNSS, R_{IMU}^e is the position vector of IMU in the geocentric earth-fixed coordinate system, and r_{GNSS}^e is the position vector of GNSS in the geocentric earth-fixed coordinate system.

There is a difference in the length of the arm between GNSS and IMU, and there is also a difference in the speed of the two when the carrier moves. To integrate GNSS and IMU data, GNSS information needs to be transformed to unify the reference benchmark.

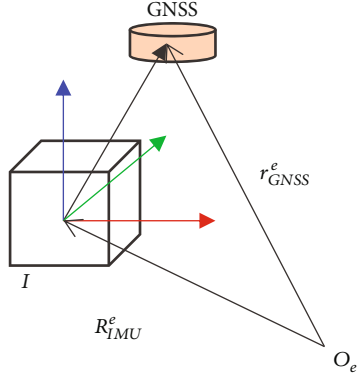


FIGURE 3: GNSS arm lever effect reduction correction.

In the geocentric earth-fixed coordinate system, the position vector of GNSS can be expressed as r_{GNSS}^e , and the position vector of IMU is r_{IMU}^e . Then, the position difference between GNSS and IMU, namely, the length of the space arm, is

$$\delta l = r_{GNSS}^e - R_{IMU}^e. \quad (21)$$

In the local navigation coordinate system, there are

$$\delta l^n = [\delta L_E \quad \delta L_N \quad \delta L_H]^T = C_n^b \delta l^b. \quad (22)$$

Therefore, the relationship between GNSS observation result reduction and correction to the inertial navigation coordinate system is

$$\begin{cases} L_{IMU} = L_{GNSS} - \frac{\delta L_N}{R_{Mh}}, \\ \lambda_{IMU} = \lambda_{GNSS} - \frac{\delta L_E \sec L}{R_{Nh}}, \\ h_{IMU} = h_{GNSS} - \delta L_H. \end{cases} \quad (23)$$

In general, the installation positions of GNSS receiving antenna and IMU do not change, which can be regarded as a constant value. Then, the derivative of the relative geocentric earth-fixed coordinate system on both sides of Equation (21) is obtained:

$$\frac{d\delta l}{dt} = \frac{dr_{GNSS}^e}{dt} - \frac{dr_{IMU}^e}{dt}. \quad (24)$$

Note dr_{IMU}^e/dt as $v_{en(IMU)}$ and dr_{GNSS}^e/dt as $v_{en(GNSS)}$. The above equation projects to the inertial navigation coordinate system, where

$$\delta v_l^n = v_{en(GNSS)} - v_{en(IMU)} = C_n^b (\omega_{eb}^b \times) \delta l^b. \quad (25)$$

4.2.2. Target Observation. In the initial calculation of the mobile LiDAR, although the long-term lack of GNSS signals caused a severe drift in navigation trajectory information, the trajectory maintained a relatively high accuracy within

a short time interval within the target range. According to the graphic characteristics of the mobile LiDAR graphical target, the center coordinates of the target and the corresponding UTC time can be obtained semiautomatically with manual assistance. Since the obtained characteristic coordinate points of the graphical target have both the UTC time reference and the spatial reference of the global coordinate system after precision measurement, it can provide constraints on the spatial reference of the mobile LiDAR system and improve the accuracy of obtaining spatial information of the system.

After calculating the point cloud for the first time, according to the target center positioning method in the literature [13], firstly, the point cloud scene is manually viewed and the range of the graphic target is selected. Secondly, the target center point and its corresponding UTC time are determined according to the iterative center positioning estimated by M . Finally, according to other measurement methods, the actual precise coordinates of the graphical target in the scene are obtained.

According to the LiDAR positioning geometric model, the laser scanner rotates at high speed to obtain the coordinate X_L of the point cloud in the scanning coordinate system. The coordinates of the laser foot point in the WGS-84 coordinate system can be measured according to the placement parameters, the estimated IMU center position, and the estimated attitude by POS system. The positioning geometric equation is shown in

$$X_{WGS-84} = R_N [R_M X_L + X_I^L] + X_{IMU}, \quad (26)$$

where X_{WGS-84} is the coordinates of the WGS-84 coordinate system of the center foot point of the target, X_{IMU} is the measurement center of inertial measurement unit, R_N is the attitude estimation of POS system, and R_M and X_I^L are the placement rotation matrix and eccentricity of the placement parameters, respectively.

The target center coordinate X_{WGS-84}' was obtained according to the traditional measurement method, and then, the inertial measurement center coordinate could be obtained by reverse calculation, as shown in

$$X_{IMU} = X_{WGS-84}' - R_N [R_M X_L + X_I^L]. \quad (27)$$

By integrating the GNSS and target measurement information, the measurement equation of Kalman filter in the combined system can be obtained as follows:

$$Z = \begin{bmatrix} v_{IMU} - v_{GNSS} \\ X_{IMU} - X_{GNSS} \\ X_{IMU} - X_T \end{bmatrix}. \quad (28)$$

5. Experiment Analysis

To verify the effectiveness of the proposed method in this paper, two sets of experiments were adopted for verification. In the first experiment, the authors obtain the real trajectory

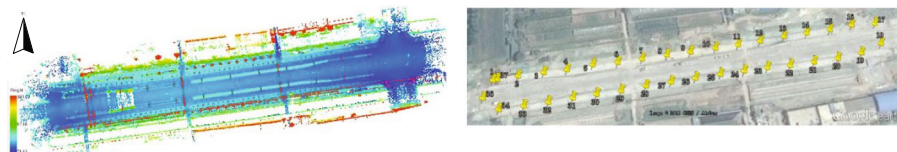


FIGURE 4: Point cloud and target arrangement in test area 1.

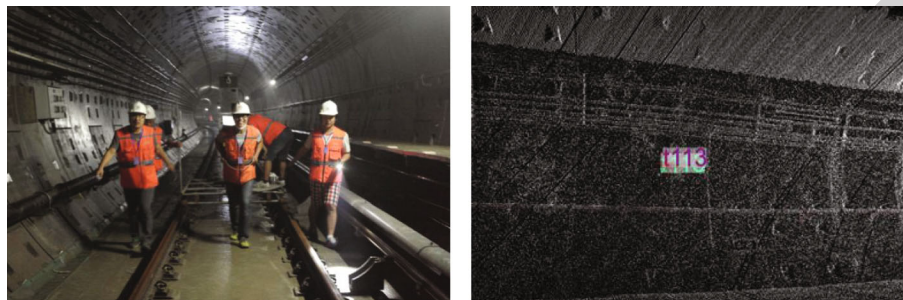


FIGURE 5: Data acquisition and target arrangement in test area 2.

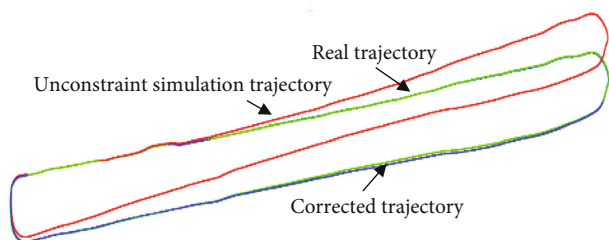


FIGURE 6: Simulated trajectory and real trajectory.

in the open-air environment, and the GNSS signal was removed artificially to verify the degree of conformity between the calculated trajectory and the real trajectory under target constraints. In the second experiment, the authors collected the data in the subway tunnels without GNSS signal and then compared and analyzed the measured values based on target constraints and the total station observations, and the degree of coincidence of the two test results was verified.

5.1. Experimental Scheme. Experiment 1: the test area is located in the newly built road environment in Jiaozuo High-tech Zone, Henan Province, with a length of 400 m. The portable flatbed vehicle is used to carry the SSW-3 mobile LiDAR system. Data are collected along nonmotorized lanes on both sides of the road. The test area is open over the sky, and there are no surrounding environments such as tall buildings and water areas that have adverse factors on GNSS signals. Plane graphical targets were set at 25 m intervals along the edge of the road, and the coordinates of the target center were accurately measured by the total station with the measurement error less than 2 cm. The time of data acquisition was October 2018, GNSS frequency was 10 Hz, IMU frequency was 200 Hz, data acquisition time was 1878 s, and the trajectory length was 836 m. Figure 4 shows the point cloud image and target layout in the test area.

Experiment 2: the test area is located in a section of Beijing Metro Line 15. A rail car was used to carry the same type of mobile LiDAR system. The data was collected by manually dragging along the track. Cross-shaped plane targets are arranged at 50 m intervals on the tunnel wall. The center point of each plane target is precisely measured by the total station, and the measurement error is less than 2 cm. The time of data acquisition was August 2014, GNSS frequency was 10 Hz, IMU frequency was 200 Hz, the data acquisition time was 270 s, and the track length was 1700 m. Figure 5 shows the data collection status and target cloud in the test area.

The data solutions of the two test areas are similar, so this study focuses on the data of the test one for analysis and research.

5.2. Data Calculation. According to the trajectory processing method, it mainly includes POS trajectory precalculation, point cloud preliminary calculation and target point cloud center location, POS trajectory calculation with cooperative target constraint, and point cloud generation.

5.2.1. POS Trajectory Precalculation. In the first experiment, the POS system acquired complete GNSS information and IMU information, and this paper used Kalman filter to obtain the complete trajectory as a reference. The maximum errors of E (east), N (north), and H (height) in the trajectory calculation were 0.003 m, 0.004 m, and 0.010 m, respectively. Then, GNSS information is ignored to obtain the trajectory calculated only by IMU, which is used as the simulated trajectory of underground space without target constraints. In the simulation environment, because the drift error in POS system cannot be effectively suppressed, the E , N , and H errors of trajectory calculation are 8.523 m, 6.522 m, and 1.122 m, respectively. The results are shown in Figure 6. It can be seen that there is a large deviation between the above two scenarios over time.

TABLE 1: Accuracy statistics of underground simulated state.

ID	1	2	3	4	5	6	7	8	9	10	11
Δx	0.041	-0.026	0.189	0.163	0.378	0.305	0.379	0.211	-0.131	-0.268	-0.399
Δy	0.014	-0.001	0.167	0.478	1.051	1.983	3.150	5.095	6.999	9.158	9.259
Δz	0.000	-0.013	0.024	0.051	0.084	0.109	0.145	0.156	0.178	0.176	0.181
Δp	0.043	0.029	0.253	0.508	1.120	2.009	3.176	5.102	7.002	9.164	9.269
ID	12	13	14	15	16	17	18	19	20	21	22
Δx	-0.668	-0.557	-0.955	-0.835	-1.064	-1.394	-1.295	0.293	0.426	0.303	0.413
Δy	11.277	11.431	13.751	13.799	14.738	17.892	18.478	19.922	19.900	18.898	18.837
Δz	0.172	0.194	0.209	0.210	0.217	0.229	0.215	0.127	0.121	0.071	0.057
Δp	11.298	11.446	13.786	13.826	14.778	17.948	18.525	19.925	19.905	18.901	18.842
ID	23	24	25	26	27	28	29	30	31	32	33
Δx	0.393	0.252	0.355	0.236	0.288	0.423	0.480	0.371	0.601	0.517	0.683
Δy	17.668	17.606	16.048	14.392	12.499	12.375	11.054	10.595	9.004	8.707	6.823
Δz	0.030	0.035	0.003	-0.032	-0.062	-0.072	-0.076	-0.076	-0.045	-0.083	-0.078
Δp	17.672	17.608	16.052	14.394	12.502	12.382	11.065	10.602	9.024	8.723	6.858

ID: the target number; Δx is the east error; Δy is the north error; Δz is the height error; Δp is the point error.

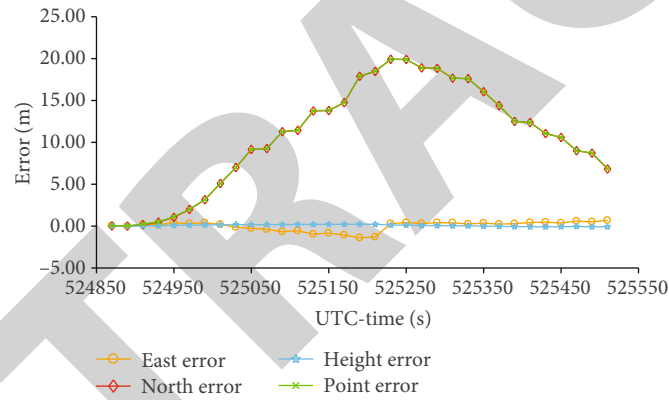


FIGURE 7: Accuracy results of underground simulated state.

5.2.2. Point Cloud Precalculation and Target Center Location. In the environment of simulated GNSS signal absence, the calculated point cloud trajectory is seriously deviated due to the lack of GNSS correction for IMU drift and other errors, and the calculated point cloud based on the pose information provided by IMU has a great deviation. However, the data acquisition time of each cooperative target data is very short. In a limited period of time, the pose calculated by IMU data still has high relative accuracy, and each target cloud has high overall consistency. According to the robust target center extraction algorithm, relatively reliable target center coordinates can be obtained at this time.

5.2.3. Trajectory Solution of Cooperative Target Constraint. According to the target cloud extracted from the precalculated point cloud, the center coordinates of the target and the measurement results of the laser scanner at the corresponding UTC time were determined. Then, according to the observation model, the known reference points of the trajectory are calculated and the trajectory is drift constrained. The blue line

in Figure 6 is the corrected track. It can be seen that the corrected track has a high degree of coincidence with the real track, which greatly improves the reliability of the track.

5.2.4. Point Cloud Solution. According to the pose information provided by the corrected trajectory, the mobile LiDAR point cloud was recalculated to obtain reliable point cloud information without GNSS signal. In this study, the length of the test area was 400 m, and the targets were arranged on both sides of the road. A total of 37 targets were set, and each target interval was 25 m. Finally, the integrated navigation trajectory is solved according to the intervals of 25 m, 50 m, 100 m, and 200 m, and the target point cloud data is finally obtained to evaluate the accuracy of the constrained point cloud results.

5.3. Constraint Results and Analysis. In the simulation of GNSS signal-free state, the error of pose estimation by IMU appears to drift over time. The deviations between the calculated coordinates and the measured coordinates of the 33 cooperative target centers are shown in Table 1. The mean point-to-point errors in x , y , and z directions are

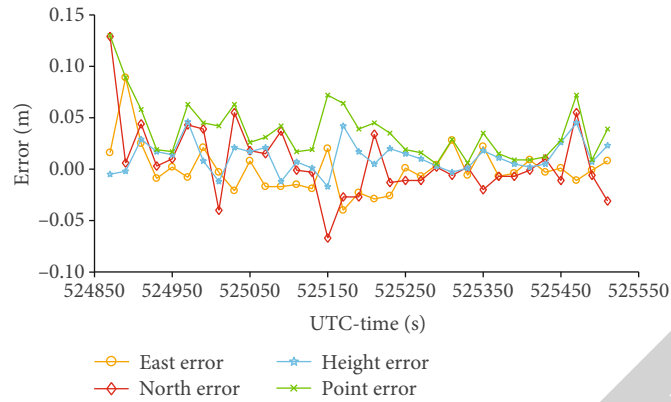


FIGURE 8: Point error under the target constraint of 25 m interval.

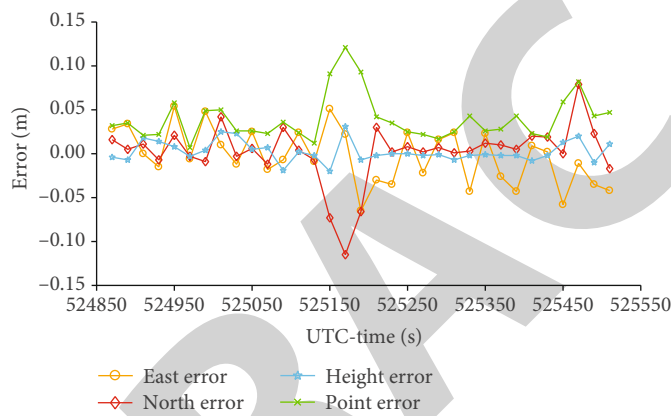


FIGURE 9: Point error under the target constraint of 50 m interval.

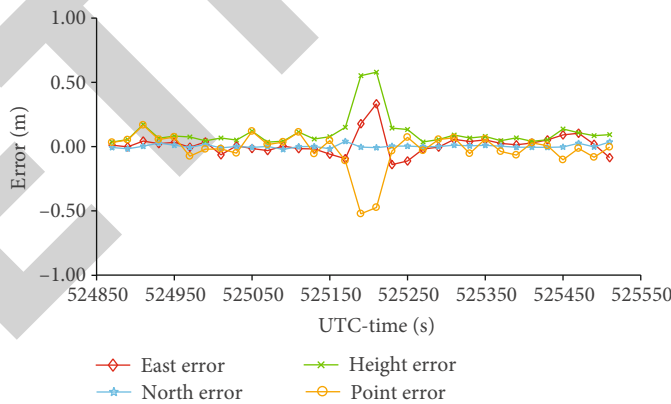


FIGURE 10: Point error under the target constraint of 100 m interval.

0.564 m, 10.698 m, and 0.010 m, respectively. The maximum point deviation is 19.925 m. The position deviation of each point is shown in Figure 7. The test track adopts a closed route. The farther away from the starting point, the greater the point error caused by IMU drift.

Target intervals of 25 m, 50 m, 100 m, and 200 m were, respectively, used to constrain the trajectory, and the point position errors obtained are shown in Figures 8–11.

From the analysis of the two test results, in the absence of GNSS signal, the trajectory of the mobile LiDAR system

accumulates with time, and the measurement error increases rapidly. Based on the algorithm in this paper, the measurement error decreases rapidly under the constraint of cooperative target, and the two test results are consistent. The smaller the cooperative target interval is, the smaller the measurement error value is. When the cooperative target interval is about 50 m, the measurement error can meet the requirements of general indoor space measurement. With the increase of the interval, the accuracy and instability of the measurement error gradually increase.

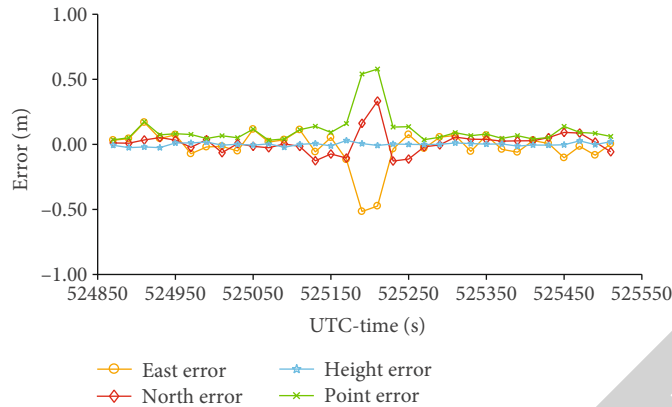


FIGURE 11: Point error under the target constraint of 200 m interval.

In the second experiment, the point cloud was solved. Without target constraint, the coordinates of 34 target points were compared with the measured values, and the mean point median errors in the x , y , and z directions were 4.076 m, 12.099 m, and 9.343 m, respectively. The proposed method was used to eliminate some unqualified targets and constrain the trajectory based on the measured target values. After recalculation, the median errors of the point cloud coordinates and the measured values were 0.051 m, 0.162 m, and 0.096 m in the x , y , and z directions, respectively.

6. Conclusion

Aiming at the measurement problem of mobile LiDAR in underground space without GNSS signal, this paper analyzes the error sources of mobile LiDAR system and concludes that the dead position and attitude error calculated by IMU is the main error source of underground mobile LiDAR. In the loose coupling mode, the trajectory error solving model based on the graphical target constraint is derived. The algorithm in this paper is verified by simulating the environment without GNSS signal and the real subway tunnel scene, respectively. The research shows that the estimated trajectory error of mobile LiDAR increases rapidly with time in the absence of GNSS signal. With the constraint of target, the measurement error can be effectively controlled. When the distance between the graphic targets is about 50 m, a more stable and reliable measurement result can be obtained. Based on the error correction of the target constraint, although it can achieve effective correction of the pose to a certain extent, each graphical target only can be used as an effective constraint point, which has limited restraint ability on the estimated trajectory and less restraint on the posture. In the later study, the cooperative target and the corresponding correction model will be expanded to apply to more complex environment. And a more robust correction model that can simultaneously correct the pose will be adopted.

Data Availability

The data that support the findings of this study are available within the article.

Conflicts of Interest

The authors declare that they have no competing interest.

Authors' Contributions

Huiyun Liu and Yongqiang Li contributed equally to this work as co-first author.

Acknowledgments

This work was supported by the National Natural Science Foundation (41771491).

References

- [1] Y. Han, H. Sun, and R. Zhong, "Three-dimensional linear restoration of a tunnel based on measured track and uncontrolled mobile laser scanning," *Sensors*, vol. 21, no. 11, p. 3815, 2021.
- [2] W. Gu and H. Tang, "Methodology for collecting underground spatial survey data in Shanghai and an assessment of their accuracy," *Shanghai Land and Resources*, vol. 35, no. 2, pp. 74–78, 2014.
- [3] G. Fotopoulos and M. E. Cannon, "An overview of multi-reference station methods for cm-level positioning," *GPS Solutions*, vol. 4, no. 3, pp. 1–10, 2001.
- [4] S. Tian, X. Ge, and Z. Tu, "Testing study on digital close-range photogrammetry for measuring deformations of tunnel and underground spaces," *Chinese Journal of Rock Mechanics and Engineering*, vol. 25, no. 7, pp. 1309–1315, 2006.
- [5] D. Zhang, K. Chen, and Z. Ma, "Underground intelligent laser scanning system," *China Mining Magazine*, vol. 23, Supplement 1, pp. 207–212, 2014.
- [6] Y. F. Mao, H. Li, and B. Yang, "A directed-line-segment-based photogrammetry method to survey the tunneling working surface of mine roadway," *Journal of the Indian Society of Remote Sensing*, vol. 46, no. 2, pp. 189–198, 2018.
- [7] Y. Li, Z. Guo, H. Liu, L. Niu, and Y. Yan, "Development of underground space transportable laser surveying system," *Coal Mining Technology*, vol. 21, no. 2, pp. 83–86, 2016.
- [8] N. Liu, *Methods of Improving Calculation Accuracy of Trajectory in Vehicle-Borne LiDAR*, Henan Polytechnic University, Jiaozuo, 2011.

- [9] M. Joerger and B. Pervan, "Measurement-level integration of carrier-phase GPS and laser-scanner for outdoor ground vehicle navigation," *Journal of Dynamic Systems Measurement and Control*, vol. 131, no. 2, pp. 1–11, 2009.
- [10] P. D. Groves, *Principles of GNSS, Inertial, and Multisensory Integrated Navigation Systems*, Artech house, 2013.
- [11] R. Hung, B. King, and W. Chen, "Conceptual issues regarding the development of underground railway laser scanning systems," *ISPRS International Journal of Geo-Information*, vol. 4, no. 1, pp. 185–198, 2015.
- [12] D. Zhang, *Research on System Consistency and Optimal States Estimation of LIDAR/INS Integrated Navigation System*, National University of Defense Technology, Beijing, 2010.
- [13] Y. Lv, Y. Li, Q. Yang, and P. Li, "Robust plane target center location algorithm based on M estimation," *Science Technology and Engineering*, vol. 19, no. 3, pp. 6–11, 2019.
- [14] P. Sun, *Research on Key Techniques of Underground Mobile Laser Measurement System*, Henan Polytechnic University, Jiaozuo, 2014.
- [15] C. Qian, *Research on GNSS/INS/LiDAR High Precision Positioning Method in Weak GNSS Signal Region and Its Application*, Wuhan University, Wuhan, 2017.
- [16] X. Deng, N. Xu, and B. Jia, "Application of SSW system in 3D modeling of underground large parking lot," *Geomatics World*, vol. 26, no. 5, pp. 53–57, 2019.
- [17] T. Yu, *Algorithm Improvement of Indoor Simultaneous Location and Mapping (SLAM) Based on LiDAR/INS Integration*, Wuhan University, Wuhan, 2017.
- [18] Z. Li, Z. Hou, J. He, and Z. Liu, "Discussion on the method pattern of underground space data acquisition in backpack laser scanning system," *Bulletin of Surveying and Mapping*, pp. 141–144, 2020.
- [19] P. Schaer and J. Vallet, "Trajectory adjustment of mobile laser scan data in GPS denied environments," *The International Archives of the Photogrammetry, Remote Sensing and Spatial Information Sciences*, vol. XL-3/W4, pp. 61–64, 2016.
- [20] A. Soloviev, "Tight coupling of GPS, laser scanner, and inertial measurements for navigation in urban environments," in *2008 IEEE/ION Position, Location and Navigation Symposium*, Monterey, CA, USA, 2008.
- [21] Y. Gao, S. Liu, M. M. Atia, and A. Noureldin, "INS/GPS/LiDAR integrated navigation system for urban and indoor environments using hybrid scan matching algorithm," *Sensors*, vol. 15, no. 9, pp. 23286–23302, 2015.
- [22] L. Chang, X. Niu, T. Liu, J. Tand, and C. Qian, "GNSS/INS/LiDAR-SLAM integrated navigation system based on graph optimization," *Remote Sensing*, vol. 11, no. 9, p. 1009, 2019.
- [23] L. Chang, X. Niu, and T. Liu, "GNSS/IMU/ODO/LiDAR-SLAM integrated navigation system using IMU/ODO pre-integration," *Sensors*, vol. 20, no. 17, p. 4702, 2020.
- [24] W. Liu, Z. Li, S. Sun, M. Gupta, H. Du, and R. Malekian, "Design a novel target to improve positioning accuracy of autonomous vehicular navigation system in GPS denied environments," *IEEE Transactions On Industrial Informatics*, vol. 17, no. 11, pp. 7575–7588, 2021.
- [25] S. Liu, J. Luo, J. Hu, H. Luo, and Y. Liang, "Research on NDT-based positioning for autonomous driving," *E3S Web of Conferences*, vol. 257, article 02055, 2021.
- [26] M. Chung, C. Kim, K. Choi, D. Chung, and Y. Kim, "Development of LiDAR simulator for backpack-mounted mobile indoor mapping system," *Journal of the Korean Society of Surveying, Geodesy, Photogrammetry and Cartography*, vol. 35, no. 2, pp. 91–102, 2017.
- [27] C. Kanellakis, P. S. Karvelis, S. S. Mansouri, A. A. Agha-Mohammadi, and G. Nikolakopoulos, "Towards autonomous aerial scouting using multi-rotors in subterranean tunnel navigation," *IEEE Access*, vol. 9, pp. 66477–66485, 2021.
- [28] S. Khattak, *Multi-Modal Landmark Detection and Tracking for Odometry Estimation in Degraded Visual Environments*, University of Nevada, Reno, 2017.
- [29] S. Mansouri, C. Kanellakis, P. Karvelis, D. Kominiak, and G. Nikolakopoulos, "MAV navigation in unknown dark underground mines using deeping learning," in *2020 European Control Conference (ECC)*, St. Petersburg, Russia, 2020.
- [30] C. Kanellakis, S. Mansouri, G. Georgoulas, and G. Nikolakopoulos, "Towards autonomous surveying of underground mine using MAVs," in *International Conference on Robotics in Alpe-Adria Danube Region*, Cham, 2018.
- [31] L. Markovic, M. Kovac, R. Milijas, M. Car, and S. Bogdan, "Error state extended Kalman filter multi-sensor fusion for unmanned aerial vehicle localization in GPS and magnetometer denied indoor environments," 2021, <http://arxiv.org/abs/2109.04908v1>.
- [32] X. Cheng, X. Hu, K. Tan, L. Wang, and L. Yang, "Automatic detection of shield tunnel leakages based on terrestrial mobile LiDAR intensity images using deep learning," *IEEE Access*, vol. 9, pp. 55300–55310, 2021.
- [33] A. Soloviev, D. Bates, and F. Van Graas, "Tight coupling of laser scanner and inertial measurements for a fully autonomous relative navigation solution," *Navigation*, vol. 54, no. 3, pp. 189–205, 2007.
- [34] J. Tang, Y. Chen, X. Niu et al., "LiDAR scan matching aided inertial navigation system in GNSS-denied environments," *Sensors*, vol. 15, no. 7, pp. 16710–16728, 2015.
- [35] G. Hemann, S. Singh, and M. Kaess, "Long-range GPS-denied aerial inertial navigation with LIDAR localization," in *2016 IEEE/RSJ International conference on intelligent robots and systems (IROS)*, Daejeon, Korea (South), 2016.
- [36] Y. Wu, C. Wu, and X. Chen, "Introduction of several indoor positioning technology," *Geonews*, vol. 29, no. 3, pp. 1-2, 2008.
- [37] B. Liu, Q. Song, and S. Hu, "Design of the intellectual management of parking lot based on RFID," *Computer & Digital Engineering*, vol. 36, no. 5, pp. 153–155, 2008.
- [38] A. Chen, S. Li, and J. Zhang, "Mine safe monitoring wireless network based on the ZigBee technology," *Journal of Test and Measurement Technology*, vol. 22, no. 3, pp. 245–249, 2008.
- [39] Q. Luo and B. Han, "Distance and azimuth testing system based on ultrasonic and infrared detecting technology," *Computer Automated Measurement & Control*, vol. 13, no. 4, pp. 304–334, 2005.
- [40] Z. Yuan, *Analysis and Reach on Bluetooth of Short Distance Wireless Local Area Network*, Wuhan University of Technology, Wuhan, 2006.
- [41] M. Tanigawa, J. D. Hol, F. Dijkstra, H. Luinge, and P. Slycke, "Augmentation of low-cos GPS/MEMS INS with UWB positioning system for seamless outdoor/indoor positioning," in *Proceedings of the 21st international technical meeting of the satellite division of the institute of navigation (ION GNSS 2008)*, pp. 1804–1811, Savannah, GA, 2008.
- [42] Z. Liang, *Accuracy Improvement for Mobile Mapping in Complex Ground Enviroments*, Wuhan University, Wuhan, 2015, pp. 1-106.

- [43] A. Habib, K. In Bang, A. P. Kersting, and D. Lee, "Error budget of LiDAR systems and quality control of the derived data," *Photogrammetric Engineering & Remote Sensing*, vol. 75, no. 9, pp. 1093–1108, 2009.
- [44] X. Li and Z. Ni, "Research on calibration field designing for IMU/DGPS supported photogrammetry," *Engineering of Surveying and Mapping*, vol. 14, no. 4, pp. 14–18, 2005.
- [45] X. Tu, M. Xu, and L. Liu, "The geometric calibration of airborne three-line-scanner ADS40," *Acta Geodaetica et Cartographica*, vol. 40, no. 1, pp. 78–83, 2011.
- [46] M. Cramer and D. Stallmann, "System calibration for direct georeferencing," *International Archives of Photogrammetry Remote Sensing and Spatial Information*, vol. 34, no. 3, pp. 79–84, 2002.
- [47] H. Burman, "Adjustment of laser scanner data for correction of orientation errors," *International Archives of Photogrammetry Remote Sensing and Spatial Information*, vol. 33, pp. 125–132, 2000.
- [48] G. Panahandeh and M. Jansson, "IMU-camera self-calibration using planar mirror reflection," in *2011 International Conference on Indoor Positioning and Indoor Navigation*, Guimaraes, Portugal, 2011.
- [49] J. Lobo and J. Dias, "Relative pose calibration between visual and inertial sensors," *The International Journal of Robotics Research*, vol. 26, no. 6, pp. 561–575, 2007.
- [50] Z. Ye, Y. Yang, W. Zhao, and H. Yanfang, "Dynamic calibration of exterior orientations for vehicle GPS/IMU/LS laser imaging system," *Acta Geodaetica et Cartographica Sinica*, vol. 40, pp. 345–350, 2011.
- [51] G. Yao, H. Shao, H. Shao, J. Liu, Z. Pan, and J. Chen, "Multi-sensor closed-loop calibration technology for mobile measurement based on high precision POS," in *Symposium on Inertial Technology and Intelligent Navigation*, pp. 281–286, Kunming City, Yunnan Province, China, 2019.
- [52] D. Li, *The Research on Multi-Sensors Calibration of Mobile*, Xiamen University, Xianmen, 2014.